






Anomalous lattice thermal conductivity of quasi-one-dimensional palladium thiophosphate $A_2\text{PdPS}_4\text{I}$ ($A = \text{K}, \text{Rb}, \text{Cs}$)

Feng Xiao ^{1,2}, Qing-Yu Xie ^{2,3}, Xing Ming ⁴, Huashan Li ^{1,*}, Junrong Zhang,^{2,5} and Bao-Tian Wang ^{2,5,6,†}

¹*School of Physics, Sun Yat-Sen University, Guangzhou 510275, China*

²*Institute of High Energy Physics, Chinese Academy of Science, Beijing 100049, China*

³*School of Physics and Optoelectronics, Xiangtan University, Xiangtan 411105, China*

⁴*College of Physics and Electronic Information Engineering, Guilin University of Technology, Guilin 541004, People's Republic of China*

⁵*Spallation Neutron Source Science Center, Dongguan 523803, China*

⁶*Collaborative Innovation Center of Extreme Optics, Shanxi University, Taiyuan 030006, China*



(Received 16 April 2024; revised 31 May 2024; accepted 3 June 2024; published 17 June 2024)

The quest for intrinsically low lattice thermal conductivity (κ_L) has gained widespread attention in thermoelectrics and refractories. The reduction of κ_L in low-dimensional systems typically arises from anharmonicity and anisotropic chemical bonding. Due to the structural instability and the technical complexity, the thermal functional application of practical low-dimensional materials confronts great challenges. In this context, the investigations of quasi-low-dimensional bulk materials, rather than the real low-dimensional materials, hold paramount importance from both fundamental and practical perspectives. Here, we employ the *ab initio* self-consistent phonon (SCPH) theory in combination with the compressive sensing lattice dynamics method to explore the lattice dynamics and microscopic mechanisms of thermal transport in emerging pentanary thiophosphates $A_2\text{PdPS}_4\text{I}$ ($A = \text{K}, \text{Rb}, \text{Cs}$). These compounds feature covalent one-dimensional (1D) chains, providing bonding heterogeneity and resulting in flat phonon bands and low phonon group velocities (V_{ph}). The strengthened anharmonicity stems from the cooperative rattlinglike vibrations of the interchain alkali metal atoms and I atoms. In K- and Rb-containing systems, the cooperative vibrations of the rattling unit (K/Rb-I) result in strong anharmonicity, while in Cs-containing system, the abnormally enhanced rattlinglike κ_L (κ_p) is due to the antibonding interaction breaking the cooperative vibration of the rattling unit (Cs-I), thereby weakening the anharmonicity. Upon heating, the κ_p show decreasing behavior. However, the wavelike κ_L (κ_c) exhibits a positive temperature dependence, highlighting the nonnegligible coherent phonon contributions to the κ_L and triggering anomalous temperature-dependent behavior of κ_L . Our study uncovers the multifaceted microscopic mechanisms behind the low κ_L in three quasi-one-dimensional (Q-1D) systems of $A_2\text{PdPS}_4\text{I}$ and provides fresh insights for the discovery and design of Q-1D low κ_L materials.

DOI: [10.1103/PhysRevB.109.245202](https://doi.org/10.1103/PhysRevB.109.245202)

I. INTRODUCTION

Intrinsic low lattice thermal conductivity (κ_L) is an interesting feature for some solid crystalline materials and has important applications in the fields of thermoelectric [1], thermal barrier coating [2], and thermal insulation [3]. Proposed concepts for reducing κ_L of crystal include phonon-glass-electron-crystal [4], nanostructuring [5], alloying [6], entropy engineering [7], resonant bonding [8], strengthening phonon anharmonicity [9–11], and lowering dimensionality [12,13], etc. Therein, phonon anharmonicity can emerge in real materials with lone pair electrons, resonant bonding, and rattling vibrations [14]. The presence of lone pair electrons results in a nonlinear repulsive electrostatic force with the neighboring bonds, lowering the lattice symmetry, hindering lattice vibration, and thus inducing the bond anharmonicity. Besides, the rattling mode found in glasslike phonon states within

the host-object structures can significantly reduce the phonon lifetime (τ_q) and result in ultralow κ_L [15]. The rattling modes are normally associated with the large amplitude vibrations of the loosely bound atoms and result in distinctive features of the avoided crossing of the acoustic and optical phonon modes as well as the flat guest mode in the phonon spectrum [16]. Beyond anharmonicity, lowering dimensionality offers an effective means of modulating κ_L . Nevertheless, it is difficult to accurately measure the thermal transport properties of the real low-dimensional materials, limited by the manufacturing and technical complexity and reliability of the existing measurement devices [17]. In comparison to real low-dimensional materials, Q-1D materials are good substitutes and focusing on them holds great practical significance for experimental measurement, material design, and applications.

In quasi-two-dimensional (Q-2D) systems with the absence of dangling bonds, it is believed that the bonding heterogeneity can give rise to partially localized low-frequency phonon modes [18,19], resulting in low V_{ph} [20] and strong anharmonicity [21,22]. For instance, due to of the

*Contact author: lihsh25@mail.sysu.edu.cn

†Contact author: wangbt@ihep.ac.cn

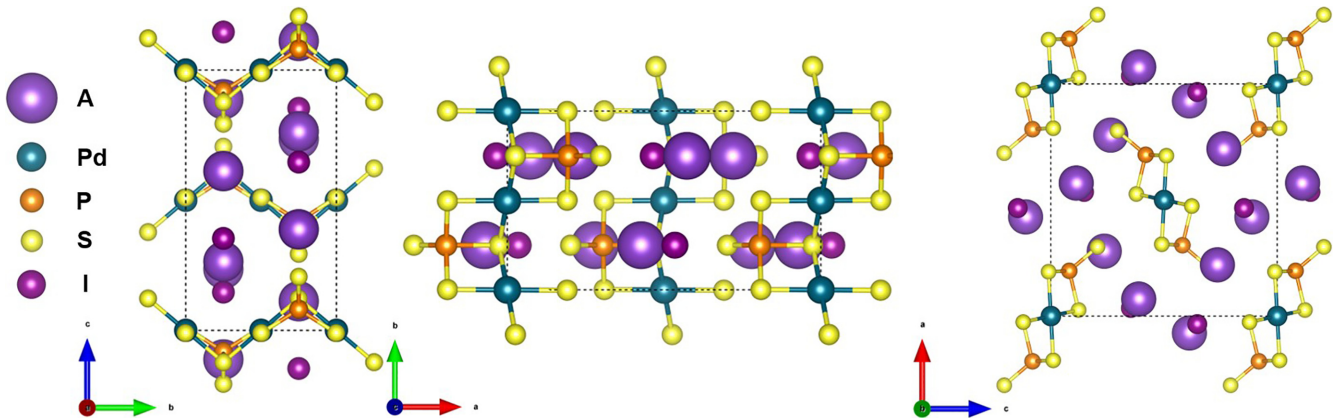


FIG. 1. Crystal structure of A_2PdPS_4I viewed along different crystalline directions. The violet, dark cyan, orange, yellow, and purple balls represent the A (K, Rb, and Cs), Pd, P, S, and I atoms, respectively. The black dotted frames represent the unit lattice.

layered structure and weak bonding, the out-of-plane κ_L of SnSe approaches the amorphous limit ($<0.2 \text{ W m}^{-1} \text{ K}^{-1}$) at $\sim 800 \text{ K}$ [23]. Likewise, the weakly bound interaction of BiCuSeO results in low stiffness, fairly large Gruneisen parameter (γ), and low κ_L of $0.88 \text{ W m}^{-1} \text{ K}^{-1}$ at 300 K [24]. Simultaneously, the low-dimensional structures deriving from these multistage bonds can also induce certain low-dimensional characteristics in terms of electrons and can markedly tune electrical transport properties [25]. Recent studies have indicated that such anisotropic electron and phonon transport in low-dimensional systems provide a promising avenue for decoupling the thermoelectric parameters [26]. Due to these benefits, Q-2D or layered materials have garnered wide attention in the field of thermal transport. However, investigations of the thermal transport of the Q-1D bulk materials, which exhibit similar chemical bonding nature as the Q-2D materials, are still scarce.

Q-1D bulk materials have begun to come into view and showcase fascinating thermoelectric transport properties only in recent years [17]. Notably, Dong *et al.* recently reported remarkable thermoelectric characteristics, with an application-level room temperature ZT (thermoelectric figure of merit) value of 1.3 and glasslike κ_L , in a Q-1D material $TiCu_3Te_2$ [27]. Yang *et al.* revealed that the Q-1D $SbCrSe_3$ exhibits an ultralow κ_L of $0.56 \text{ W m}^{-1} \text{ K}^{-1}$ at 900 K , which can be attributed to the anharmonic phonons with the existence of the lone pair electrons of Sb atoms and weak bond between the $CrSe_6$ double chains [28]. Q-1D materials of Ta_4SiTe_4 [29], $\alpha\text{-YbAlB}_4$ [30], and KMn_6Bi_5 [31] also show remarkable thermoelectric transport properties. Regrettably, due to the challenges in estimating the force constant in complex and low-symmetry crystal structures, the aforementioned studies have predominantly focused on electrical transport properties. Although it has been widely confirmed that the weak van der Waals (*vdW*) interactions can significantly reduce the κ_L , the anharmonic lattice dynamics and thermal transport properties of complex Q-1D materials remain elusive: (i) how do the higher-order anharmonicity couple with the harmonic phonon eigenstates, which may induce complex phonon self-energy; (ii) the understanding of the interaction mechanisms between the interchain atoms and the host chains and the resulting

origin of the anharmonicity remains stuck on phenomenal; (iii) the effect of the coherent coupling between different vibrational eigenstates induced by phonon broadening on thermal transport remains unknown due to a lack of a distinct physical picture. Therefore, the understanding of the nature of the anharmonic dynamics and the ultralow κ_L has become an urgent issue in exploring the thermal functional properties of the Q-1D bulk materials.

Recently, with the assistance of the reactive halide flux, a new pentanary thiophosphate K_2PdPS_4I was successfully synthesized [32]. K_2PdPS_4I crystallizes in the orthorhombic space group $Pnma$, characterized by infinite long 1D $[PdPS_4^-]$ chains, as illustrated in Fig. 1. The main body of the 1D chain is composed of a corner-sharing $[PdS_4]$ square planes and additional $[PS_4]$ tetrahedra. The planar tetragonal crystal field of Pd atoms constructs diamagnetic electron orbitals, hindering spin polarization, and introducing a bandgap in PdX_2 ($X = S$ or Se) [33–35]. The presence of K and I atoms within the interchain space serves to neutralize the charge [32]. Simultaneously, the relatively isolated atomic environment within the interchain space offers a stable platform for atomic-level material design. Recent work revealed its highly anisotropic elastic modulus, electrical transport, and optical properties from first-principles calculations [36]. The characteristics of the flat phonon spectrum and low-frequency acoustic branch indicate its potential of ultralow V_{ph} and κ_L . Stimulated by these phonon dynamic features as well as the special Q-1D crystal structure of K_2PdPS_4I , we extend the system to A_2PdPS_4I ($A = K, Rb, Cs$) through elemental substitution K with Rb or Cs. Such a method is a typical way to synthesize new materials. For example, the $CsCu_5S_3$ [37] and $CsCu_5Se_3$ [38] were successfully synthesized via elemental substitution following the report of $CsAg_5Te_3$ [39]. Here, we study the stability, phonon dynamic characteristics, and thermal transport properties of A_2PdPS_4I by first-principles calculations. Significant anharmonicity is found to be mainly correlated to the I and A atoms, which are weakly bonded with the 1D $[PdPS_4^-]$ chains. The κ_L values perpendicular to the chain are as low as $\sim 0.15\text{--}0.60 \text{ W m}^{-1} \text{ K}^{-1}$ in a wide temperature range. Upon heating, reduced κ_p and enhanced κ_c give a weak temperature-dependent behavior of κ_L . Overall, the low κ_L

with anomalous temperature-dependent behavior points to the potential thermal management performance of the A_2PdPS_4I in many realistic applications.

II. METHODOLOGY

A. Density-functional theory calculations

First-principles calculations are performed with the projector-augmented wave [40] method and plane-wave basis set [41], as implemented in VASP [42,43]. The cutoff energy for the plane-wave basis is set to 520 eV. The exchange-correlational interactions are simulated by the Perdew-Burke-Ernzerhof [44] functional of the generalized gradient approximation [45]. The smallest allowed spacing between \mathbf{k} points is set to 0.1 \AA^{-1} , corresponding to a \mathbf{k} point density of $10^3/\text{\AA}^{-3}$. The lattice parameters are fully optimized until the total energy and forces' convergences are less than 10^{-8} eV and 10^{-8} eV/\text{\AA}, respectively. The density-functional theory (DFT)-D3 method of Grimme with zero-damping function [46] is employed to calculate the dispersion correction term, to consider the interchain vdW interactions.

B. Extraction of force constants

The extractions of harmonic and anharmonic interatomic-force constants (IFCs) are carried out with the aid of the finite displacement approach and the compressive sensing lattice dynamics method [47], respectively, using the ALAMODE package [48] and on a $1 \times 2 \times 1$ supercell. Concretely, we use the *ab initio* molecular dynamics (AIMD) simulations at 300 K to generate 80 snapshots and specify the random displacement length as 0.08 \AA on all atoms inside the snapshot structures to capture the random displacement configurations. The energy minimization of configurations is carried out using a $4 \times 4 \times 4$ k -mesh grid until the energy change between the two steps is smaller than 10^{-8} eV. In this work, all possible harmonic terms between atoms are included, and the 15th, tenth-, fifth-, and fifth- nearest neighbors are chosen as the interaction cutoff for the third-, fourth-, fifth-, and sixth-order IFCs, respectively. Since the four-body clusters are less important than the three-body and less-body clusters, the four-body clusters are excluded in calculating the fourth-order IFCs, and the multi (>2)-body clusters are excluded in fitting the fifth- and sixth-order IFCs. The elastic net optimization is solved with a residual of less than 1.83%, to collect the anharmonic IFCs.

C. Self-consistent phonon calculation.

To renormalize phonon energies at finite temperatures, the self-consistent phonon (SCPH) method [49] is employed. If the off-diagonal (OD) elements of the self-energy are reduced, the temperature-dependent phonon frequencies can be obtained by solving the following reduced equation:

$$\Omega_q^2 = \omega_q^2 + 2\Omega_q I_q^{(a)}, \quad (1)$$

$$I_q^{(a)} = \frac{1}{2} \sum_{q_1} \frac{\hbar \Phi(\mathbf{q}; -\mathbf{q}; \mathbf{q}_1; -\mathbf{q}_1)}{4\Omega_q \Omega_{q_1}} [1 + 2n(\Omega_{q_1})], \quad (2)$$

where ω_q is the harmonic phonon frequency, Ω_q is the anharmonically renormalized phonon frequency at finite temperature (T), \hbar is the reduced Planck constant, and Φ is the reciprocal representation of the quartic IFCs. $n(\omega) = 1/[\exp(\frac{\hbar\omega}{k_B T}) - 1]$ is the phonon population that obeys the Bose-Einstein statistic. The cubic anharmonic IFCs do not significantly renormalize the phonon frequency in low κ_L systems. So its correction for harmonics is not considered [50].

D. Phonon transport

The particlelike propagation of the phonon wave packets is estimated by solving the Peierls-Boltzmann transport equation (PBTE) within the relaxation-time approximation (RTA) [51]:

$$\kappa_p^{\mu\nu}(T) = \frac{1}{VN} \sum_{q,j} c_{qj}(T) v_{qj}^\mu v_{qj}^\nu \tau_{qj}(T), \quad (3)$$

where V is the unit cell volume and N is the total number of q points, $c_{qj}(T) = \hbar \omega_{qj} \partial n_{qj} / \partial T$ is the phonon mode-specific heat, v_{qj} is the group velocity, $\tau_q = [2\Gamma_q(\Omega_q)]^{-1}$ is the phonon lifetime, and \mathbf{q} and j represent the wave vector and phonon branch, respectively. The phonon linewidth Γ_q can be obtained explicitly from the imaginary part of the phonon self-energy that results from the cubic anharmonicity [50]:

$$\begin{aligned} \Gamma_q(\omega) = & \frac{\pi}{2N} \sum_{q',q''} \frac{\hbar |\Phi(-\mathbf{q}, \mathbf{q}', \mathbf{q}'')|^2}{8\Omega_q \Omega_{q'} \Omega_{q''}} \\ & \times [(n_{q'} + n_{q''} + 1)\delta(\omega - \Omega_{q'} - \Omega_{q''}) \\ & - 2(n_{q'} - n_{q''})\delta(\omega - \Omega_{q'} + \Omega_{q''})]. \# \quad (4) \end{aligned}$$

Here, $\Phi(-\mathbf{q}, \mathbf{q}', \mathbf{q}'')$ is calculated from cubic IFCs, and Ω_q is the temperature-dependent phonon frequencies in Eq. (1). The three-phonon (3ph) phase space, determined entirely from a material's phonon dispersion, is directly related to the hardening or softening of phonons at finite temperature, given by the following equation [52]:

$$\begin{aligned} W_3^{(\pm)}(\mathbf{q}j) = & \frac{1}{N_q} \sum_{q_1, q_2, j_1, j_2} \begin{Bmatrix} n_2 - n_1 \\ n_1 + n_2 + 1 \end{Bmatrix} \\ & \times \delta(\omega_{qj} \pm \omega_{q_1 j_1} - \omega_{q_2 j_2}) \delta_{\mathbf{q} \pm \mathbf{q}_1, \mathbf{q}_2 + \mathbf{G}}. \quad (5) \end{aligned}$$

Here N_q represents the total number of wave vectors in the Brillouin zone, $\{ \frac{n_2 - n_1}{n_1 + n_2 + 1} \}$ is the Bose-Einstein distribution function to describe the phonon occupation number. Superscripts of " W^{\pm} " distinguish the processes of phonon interactions. W^+ corresponds to the combination process ($W^+ : \lambda + \lambda_1 \rightarrow \lambda_2$) where the energy of two incident phonons merge into one phonon, while W^- means the splitting process ($W^- : \lambda \rightarrow \lambda_1 + \lambda_2$) in which the energy of an incident phonon splits into two phonons. λ is the commonly used symbol to describe the scattering process, which represents a specific phonon mode.

In addition, the OD terms of the heat-flux operator, which contribute to κ_c and describe the wavelike tunneling of coherent phonons, need to be considered. κ_c is usually ignored in simple crystals because the phonons are well separated and are slightly broadened as a function of temperature.

TABLE I. Lattice constants, volume, atomic distances, and cohesive energy of pentanary thiophosphate: K_2PdPS_4I , Rb_2PdPS_4I , and Cs_2PdPS_4I .

A	Lattice constants (Å)			Volume (Å ³)	Distances (Å)				E_{coh} (eV)
	a	b	c		A-I	A-S	Pd-S	P-S	
K^{Exp} [32]	12.353	6.952	12.123	1041.1	3.434				
K^{Cal} [36]	12.348	7.018	12.113	1049.6					
K	12.354	7.024	12.094	1049.5	3.414	3.573	2.339	2.063	-4.256
Rb	12.652	7.189	12.495	1136.4	3.517	3.685	2.340	2.066	-4.247
Cs	13.029	7.418	13.008	1257.2	3.662	3.834	2.342	2.068	-4.242

Non-negligible κ_c is in the presence of a large unit cell (many closely spaced phonon branches), strong anharmonicity (large broadening of the phonon branches), or the coexistence of disorder [53,54]. Recent studies have shown that κ_c is substantial

for materials with ultralow κ_L , such as Mn_4Si_7 [55], $Ba_{7.81}Ge_{40.67}Au_{5.33}$ clathrate [56], Tl_3VSe_4 [57], and $CsPbBr_3$ [58]. Therefore, in Q-1D A_2PdPS_4I with complex construction and strong anharmonicity, we incorporate κ_c as follows:

$$\kappa_c^{\mu\nu}(T) = \frac{1}{VNq} \sum_{\substack{q, j, j' \\ j \neq j'}} \frac{c_{qj}\omega_{qj'} + c_{qj'}\omega_{qj}}{\omega_{qj} + \omega_{qj'}} v_{qj}^{\mu} v_{qj'}^{\nu} \frac{\Gamma_{qj} + \Gamma_{qj'}}{(\omega_{qj} - \omega_{qj'})^2 + (\Gamma_{qj} + \Gamma_{qj'})^2}, \quad (6)$$

where $\Gamma_{qj} = \frac{1}{\tau_{qj}}$ is the phonon linewidth (half-width) of phonon mode $\mathbf{q} j$, and v_{qj}^{ν} is the band OD generalization of the group velocity. The summation notation in Eq. (6) requires that the coherently scattered phonons pertain to different phonon modes. The κ_L is convergent in the \mathbf{q} grid of $8 \times 12 \times 8$.

E. Electrical transport

Electron transport properties such as conductivity, electron thermal conductivity, and Seebeck coefficient are calculated within the framework of the AMSET [59] package, which uses the momentum relaxation-time approximation to calculate the scatter ability and mobility within the Born approximation. The electron-acoustic phonon interaction is treated by the fully anisotropic acoustic deformation potential method [60], including the perturbations from longitudinal (transversal) modes and anisotropy in the deformation response to support the anisotropic materials. On the other hand, the electro-optical phonon interaction is treated by using the polar optical phonon method [61]. Moreover, the effect of ionized impurity scattering as well as the scattering of carriers by lattice ionization are also included. The resulting electronic relaxation times (τ) (the inverse of scattering rates) of the considered scattering processes can be written by following Matthiessen's rule:

$$\frac{1}{\tau_{\text{total}}} = \frac{1}{\tau_{ADP}} + \frac{1}{\tau_{IMP}} + \frac{1}{\tau_{POP}}. \quad (7)$$

To accurately evaluate the band gap, the Heyd-Scuseria-Ernzerhof (HSE06) hybrid functional is employed. The second-order derivatives of the total energy relative to the ion position are calculated by the finite difference method [58,62]. The dynamical matrix is constructed and diagonalized the phonon modes, to capture the dielectric tensors, the Born effective charges, and elastic tensors. The interpolation factor

controlling the interpolation density is set as 40, generating $43 \times 75 \times 43$ \mathbf{k} mesh, to ensure the accuracy of the calculated scattering rate.

III. RESULTS AND DISCUSSION

A. Crystal structures and stability

The thoroughly relaxed lattice constants are shown in Table I, and the calculated results of K_2PdPS_4I reproduce the previous experimental results [32] well. The lattice constants and volumes of these materials increase with the increase of the radius of the cation. This expansion leads to a larger distance between the alkali ions and I or S atoms, exceeding 3.4 Å, further expanding the interchain space. The isolation of the I atoms and alkali metal atoms in the interchain space is a defining characteristic of the host-guest structure, which may result in rattlinglike vibration modes [39,50].

Cohesion energy is a crucial index for assessing the thermal stability of artificially constructed materials. In solids, cohesion energy is the energy required to separate structured atoms from each other into neutral free atoms. It is defined in a cell of N atoms as follows [63]:

$$E_{\text{coh}} = \frac{1}{N} \left(\sum_{\text{atoms}} E_X - E_{\text{atom}} \right), \quad (8)$$

where E_{atom} is the total energy of the solid and E_X represents the corresponding energy of the constituent atoms. The cohesion energies of A_2PdPS_4I , as presented in Table I, are very close and comparable to those of some perovskites [64], indicating that the materials we studied are thermally stable and may be synthesized experimentally. AIMD simulations are further performed to evaluate the thermodynamic stability of A_2PdPS_4I , as shown in Fig. S1 in the Supplemental Material [65]. The continuous simulations of 4 ps at 800 K reveal that these Q-1D crystal structures are not

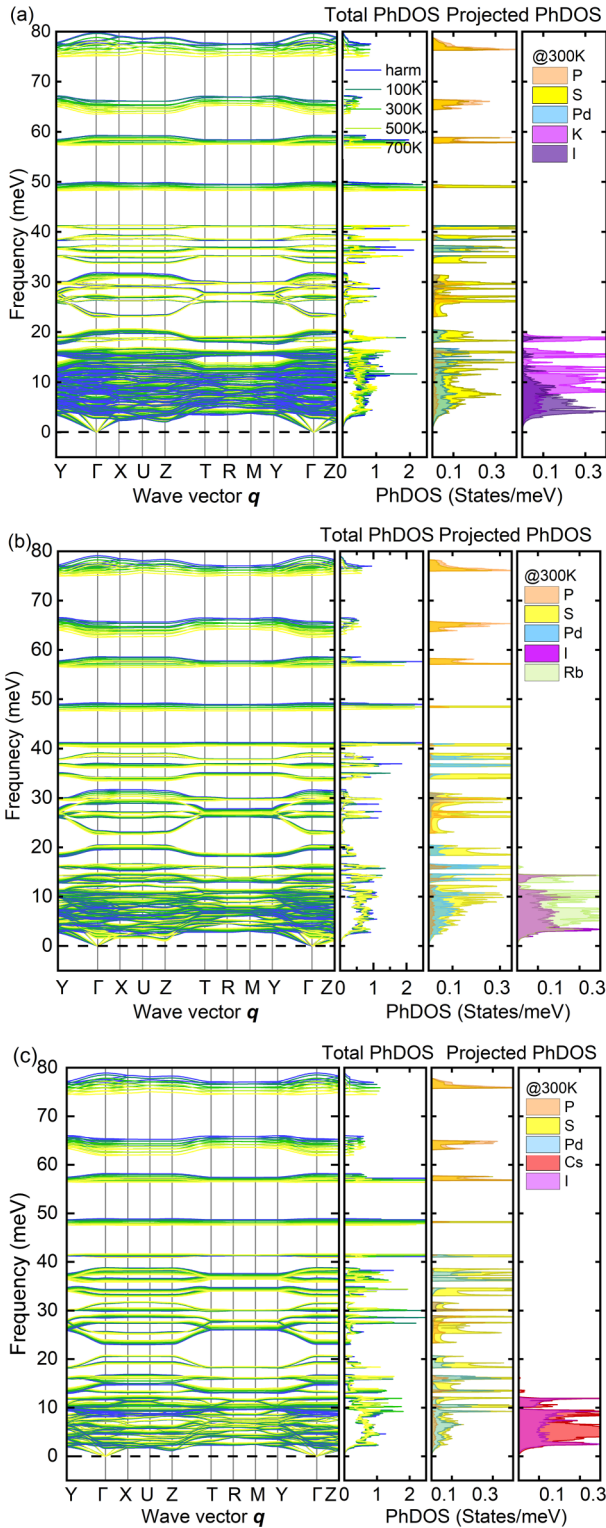


FIG. 2. Temperature-dependent phonon spectra, PhDOSs, and element-resolved PhDOSs at 300 K for (a) $\text{K}_2\text{PdPS}_4\text{I}$, (b) $\text{Rb}_2\text{PdPS}_4\text{I}$, and (c) $\text{Cs}_2\text{PdPS}_4\text{I}$.

deconstructed. Furthermore, Fig. 2 presents the phonon spectrum under harmonic approximation and anharmonic renormalization at finite temperatures, with no imaginary frequency observed, thus, confirming their dynamic stability. More

detailed discussions of the phonon dynamic will be carried out later.

The elastic properties of a lattice are characterized by its elastic constants matrix, which illustrates how the energy evolves of materials when subjected to strain. The mechanical stability of an orthorhombic system can be assessed using Born stability conditions of [36,66]:

$$C_{11} > 0, C_{44} > 0, C_{55} > 0, C_{66} > 0,$$

$$C_{11} * C_{22} > C_{12}^2,$$

$$C_{11} * C_{22} * C_{33} + 2C_{12} * C_{13} * C_{23} - C_{11} * C_{23}^2 - C_{22} * C_{13}^2 - C_{33} * C_{12}^2 > 0. \quad (9)$$

The independent elastic constants are presented in Table SI in the Supplemental Material [65]. All the elastic constants decrease with increasing atomic number of the alkali metal, reflecting the reduced stiffness. Notably, in terms of the orthogonal direction, the elastic constant along the y axis undergoes the least change, which depends heavily on the robust covalent interaction within the 1D chain. As the alkali metal ion radius increases, the interchain space expands, shear resistance diminishes, and ν increases. The diminished values of bulk modulus B , Shear modulus G , and Young's modulus E further underscore the attenuation of resistance to various deformation. These depressed elastic moduli in $\text{A}_2\text{PdPS}_4\text{I}$ substantially enhance the anharmonicity in the lattice, reduce the V_{ph} , and lower the κ_L to a large extent [67]. The visualized elastic properties are shown in Fig. S2 in the Supplemental Material [65], where high anisotropy can be found in these quasi-low-dimensional crystals. The deformation in Q-1D $\text{A}_2\text{PdPS}_4\text{I}$ occurs essentially through the arrangement of chains, and the elastic properties are expected to be dominated by weak interchain νdW forces, akin to what is the case in polymer materials [68]. What's more, defined as the ratio of B to G and utilized to evaluate the brittle or ductile (greater or less than 1.75) [69], Pugh's ratio (1.993, 2.210, and 2.432) in $\text{A}_2\text{PdPS}_4\text{I}$ ($A = \text{K}, \text{Rb}, \text{and Cs}$), exceeds 1.75 and further increases with the substitution of the alkali metal. Intrinsic softness and flexibility can accommodate a wealth of stress and strain regulation, greatly expanding their application fields and usage scenarios [36,70].

The high heterogeneity in chemical bond strength and the loose structure are the breeding grounds of low κ_L [71]. To delve further into the nature of these bonds, the crystal orbital Hamilton population (COHP) analysis is performed, focusing on the nearest-neighbor atomic pairs (Fig. S3 in the Supplemental Material [65]). The positive and negative COHP represent antibonding and bonding interactions, respectively, and a larger bonding value below the Fermi level indicates a stronger bonding interaction [72]. The intrachain S-Pd (P) bond exhibits the largest peak in COHP, which also indicates its covalent antibonding property above the Fermi energy (E_F). In contrast, the relatively small COHP of I-A (S) bonds is indicative of a weak and loose bonding of the I-A (S) bonds. Notably, below the E_F level, antibonding states stemming from Cs-I interactions appear in $\text{Cs}_2\text{PdPS}_4\text{I}$, highlighting the weakening of the bonding between these two ions.

The electron local function (Fig. S4 in the Supplemental Material [65]) also provides insights into the bonding characteristics. In the 1D chains, the shared electrons between atoms indicate strong covalent properties. The electrons in the interchain region are primarily localized on the I atom, showing almost completely stripped electrons of the alkali metal atoms. In different bonding environments, lone pair electrons are distributed around the S and I atoms. The lone pair electrons can interact with other lone pair electrons or with electrons involved in covalent bonds. This nonlinear repulsion usually hinders lattice vibration, inducing anharmonicity and reducing the κ_L [14].

B. Lattice dynamics and anharmonic phonon renormalization

The calculated phonon dispersion (Fig. 2) reveals a low cutoff frequency (<5 meV) for acoustic phonon modes, resulting in flat and low-velocity acoustic phonons. Additionally, there are several low-energy (<15 meV) optical phonon branches with inapparent dispersion. Low-energy localized phonon branches give rise to numerous phonon-scattering channels that strongly suppress κ_L in a compound [67]. The highest phonon frequencies in A_2PdPS_4I , reaching up to 80 meV, are assigned to the vibrations of the bonds between the P and S atoms outside the 1D chains. These high-frequency phonons remain insensitive to the masses of the different alkali metal atoms. The frequency of the acoustic branch decreases sequentially by about 1 meV, as the alkali metal elements transition from K to Rb and to Cs, as indicated by the enlarged phonon spectra in the low-frequency region (Fig. S5 in the Supplemental Material [65]). According to our calculated phonon density of states (PhDOSs) resolved by elements, we find that the atoms [I and A (K, Rb Cs)] located in space outside the 1D chains occupy the low-frequency region. The heavier I and A atoms participate in the low-energy modes below 20 meV. Upon heating, the phonon frequencies exhibit a strong temperature-dependent behavior: the phonons in the low-frequency region (below 20 meV) harden, while phonons in the high-frequency region (above 45 meV) soften. Unlike the other two, the lowest transverse optical branch (TO_1) of Rb_2PdPS_4I is significantly softened at the Γ point. Increasing temperature up to 700 K, no dynamic instability is observed and the overall phonon distributions in q space do not change much, indicating that all three compounds are dynamically stable over a wide temperature range and giving their practical edge.

The unique low symmetry and the loose bonding characteristics of the Q-1D structure result in the appearance of the flat optical branches in directions perpendicular to the chains, with significant phonon dispersion appearing only in the direction parallel to the 1D chains. Flat phonon dispersion always leads to low V_{ph} . Furthermore, the low-lying flat modes of the TO_1 at Γ , are predominantly governed by the parallel vibrations of the A and I atoms along 1D chains (Fig. S6 in the Supplemental Material [65]), nested with the acoustic branches. Such nesting behavior can amplify anharmonicity and provide more three-phonon (3ph) scattering channels [14,73]. Besides, localized and dispersionless phonon branching is evidence for the existence of the rattlinglike atomic vibration, a characteristic often observed in many renowned

thermoelectric materials where weakly bonded atoms hold large atomic displacement parameters [50]. The avoided crossing between the acoustic and optical modes, as illustrated in Fig. S5 in the Supplemental Material [65], serves as another indicator of the rattling vibrations. Due to the avoided crossings of phonon induced by the rattling vibrations modes, the phonon dispersion is flattened, resulting in increased phonon-phonon scattering rates and decreased V_{ph} , thereby suppressing thermal transfer [39,50].

C. Ultralow and anisotropic particlelike thermal conductivity

To elucidate the phonon thermal transport mechanism, κ_p is calculated with the harmonic or renormalized second and third IFCs, based on the PBTE method. Meanwhile, to quantify the importance of the low-frequency modes, the cumulative thermal conductivity relative to frequency is calculated. As shown in Figs. 3(a) and 3(b), if only the harmonic IFCs (Harm + 3ph) are considered, the κ_p at 300 K is underestimated seriously, compared with the results considering the quartic anharmonic renormalization (SCPH + 3ph). Specifically, compared with the results from using the SCPH, the most pronounced underestimation of κ_p under harmonic approximation is up to about 0.2 W mK^{-1} along x in K_2PdPS_4I , indicating that the low-frequency phonons hardened by the fourth anharmonic renormalization exert enormous influence on κ_p . Such a type of underestimation has also been found in $YbFe_4Sb_{12}$ [74] and Na_2KSb [75]. The discrepancy between calculated and actual κ is due to not only the neglect of anharmonic renormalization at finite temperatures but also the invalidity of the particlelike phonon picture [74]. The latter will be discussed later.

As anticipated, the κ_p of this series of materials demonstrates pronounced anisotropic properties, primarily attributed to their inherent 1D chain structure. At room temperature, the κ_p exhibits maxima along the 1D atomic chains (y axis) dominated by the covalent interactions. Conversely, in the directions perpendicular to the chain (x or z axis), due to the weak vdW interactions, the loose structure, and the repulsion of the lone pairing electrons, the thermal transport capacity is inadequate. Phonon modes below 10 meV bear more than 90% of the cumulative thermal conductivity along x or z . In the y direction, the main cumulative is extended up to 30 meV, while the contribution below 10 meV still accounts for up to two-thirds of the total κ_p . Hence, ultralow and anisotropic κ_p at room temperature ($A = K/Rb/Cs$: $\kappa_p^x = 0.458/0.075/0.102 \text{ W mK}^{-1}$, $\kappa_p^y = 1.227/0.417/0.565 \text{ W mK}^{-1}$, and $\kappa_p^z = 0.326/0.054/0.079 \text{ W mK}^{-1}$) can be found. The averaged κ_p values are $\kappa_p^K = 0.670 \text{ W mK}^{-1}$, $\kappa_p^{Rb} = 0.182 \text{ W mK}^{-1}$, and $\kappa_p^{Cs} = 0.248 \text{ W mK}^{-1}$ for A_2PdPS_4I . Especially, the values of κ_p^{Rb} and κ_p^{Cs} are much lower than those of the admitted thermoelectric materials with high performances like PbTe, SnSe, and Bi_2Te_3 [25,76–79]. As temperature increases, the κ_p values are further diminished, which is a commonly observed phenomenon in numerous materials described by the standard Peierls theory [80]. According to the Keyes expression, there exists an inverse relationship between the atomic mass or

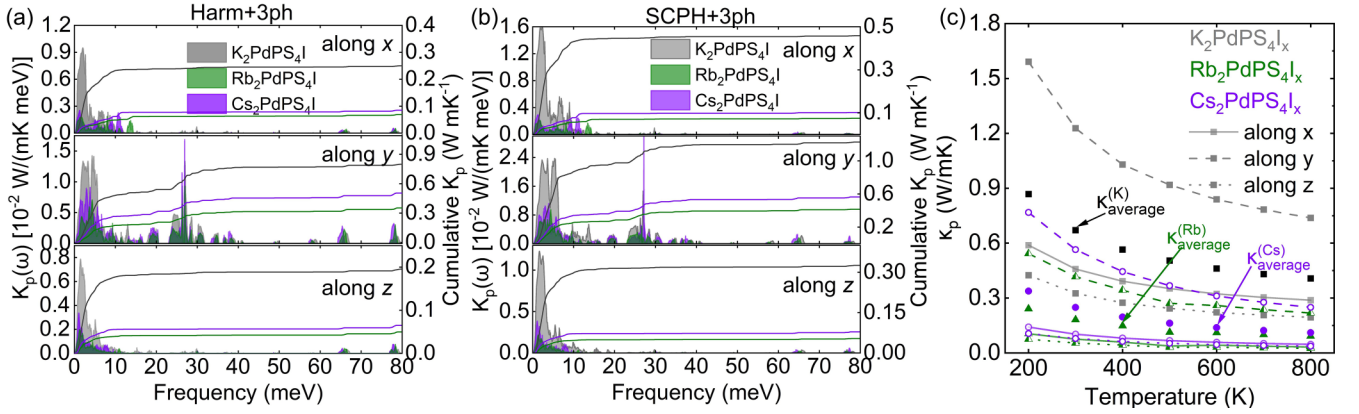


FIG. 3. Anisotropic thermal conductivity spectra and their cumulative at 300 K calculated by the (a) harmonic approximation (Harm + 3ph) and (b) anharmonic renormalization (SCPH + 3ph). (c) κ_p (calculated by SCPH + 3ph) as a function of temperature. Convergence tests of the calculated κ_p of A_2PdPS_4I along a certain direction at 300 K are shown in Fig. S7 in the Supplemental Material [65].

average atomic weight of a known compound and its κ_p [79]. Unexpectedly, Rb_2PdPS_4I demonstrates the lowest κ_p , with κ_p^y of 0.218, κ_p^x of 0.032, and κ_p^z of 0.025 $W \cdot mK^{-1}$ at 800 K. Such an anomalous trend has also been observed in several examples of chalcopyrite (space group $I-42d$) [81] and may be attributed to the softened TO_1 upon heating.

D. Abnormal phonon transport tendency

The abnormal phonon transport behaviors and their temperature dependences are closely linked to the phonon dynamics. Upon heating, the vibrations of the lowest TO modes (including TO_1 and TO_2) typically increase [50]. As depicted in Fig. 4(a), the variations of the phonon frequencies of the TO_1 and TO_2 modes follow this typical tendency for K_2PdPS_4I and Cs_2PdPS_4I . However, the trends observed in Rb_2PdPS_4I are diametrically opposite, with frequencies decreasing as temperature rises. Coupled with the enhanced phonon scattering caused by the low-lying modes, this may represent one of the main reasons for the abnormally low κ_p in Rb_2PdPS_4I .

To unveil the origin of the anomalous κ_p tendency, it is imperative to delve into the microscopic mechanism underlying κ_p . As the first term of PBTE [Eq. (3)], the total constant volume specific heat capacities are calculated to be 808.77, 811.21, and 812.13 $J K^{-1} mol^{-1}$ for K_2PdPS_4I , Rb_2PdPS_4I , and Cs_2PdPS_4I , respectively. This observation aligns with the trend of increasing mass of the element and is unlikely to contribute to the anomalous κ_p of Rb_2PdPS_4I . Another critical factor in determining κ_p is the V_{ph} . As shown in Fig. 4(b), most modes have V_{ph} below 1000 m/s. Only a few values associated with the low-frequency optical acoustic branches reach 3000 m/s. The low V_{ph} can be ascribed to the flat phonons in most q spaces. The dispersionless phonon modes would result in very low values of V_{ph} . Materials composed of heavier Rb and Cs atoms deservedly harvest lower V_{ph} . However, the influence of the phonon frequency shift caused by temperature and atomic mass on V_{ph} is not readily obvious. According to Eq. (3), in addition to V_{ph} , the phonon scattering rates are also key components for phonon transport. Calculated scattering rates, as illustrated in Fig. 4(c), align with our conjecture. Within the

low-frequency phonon region below 15 meV, where phonons govern the κ_p , the scattering in Rb_2PdPS_4I exceeds that of K_2PdPS_4I and Cs_2PdPS_4I , approaching the Cahill's limit (black line). Below 15 meV, the phonon scattering rates for all three compounds approach the Cahill's limit, rendering the possible existence of the disordered glasslike lattice vibrations [82]. The pronounced phonon scattering in Rb_2PdPS_4I indicates reduced τ_q (the reciprocal of the scattering rate). In short, the C_V and V_{ph} fail to elucidate the κ_p tendency: the lowest κ_p is found in Rb_2PdPS_4I , rather than Cs_2PdPS_4I . Thus, according to Eq. (4), the diminished κ_p in Rb_2PdPS_4I should be mainly attributed to its cubic anharmonicity (i.e., strong phonon scattering; low τ_q) [81].

To comprehend the origin of the bizarrely strong scattering rate in Rb_2PdPS_4I , the Grüneisen parameters (γ) of all three compounds are calculated and plotted in Fig. 4(d). Following the Debye-Callaway model [81,83], there is an inverse square relationship between τ_q and γ . The absolute values of γ in the low-frequency (<15 meV) zone are large for all three compounds, with many exceeding 2 and some even surpassing 8. These results indicate the presence of strong phonon anharmonicity in all three materials. Beyond 15 meV, γ are clustered around zero, indicating limited contribution of the high-frequency optical phonon modes to anharmonicity. The large negative values of γ illustrate that all three compounds may undergo negative thermal expansion upon heating [84]. The largest values of γ in Rb_2PdPS_4I and Cs_2PdPS_4I mainly manifest near the zero frequency, whereas they occur near 10 meV for K_2PdPS_4I . The predominant accumulations of γ in the low-frequency region for Rb_2PdPS_4I and Cs_2PdPS_4I elucidate their relatively low κ_p in comparison with K_2PdPS_4I . To explore in detail, the γ is further projected onto the phonon dispersions along the high-symmetry paths (see Fig. S8 in the Supplemental Material [65]). It is evident that the acoustic and the low optical phonon modes in K_2PdPS_4I possess γ values close to 0. However, in Rb_2PdPS_4I and Cs_2PdPS_4I , large negative γ can be observed in their acoustic and certain low optical phonon branches. In particular, the temperature-softened TO_1 and TO_2 phonons in Rb_2PdPS_4I at the Γ point exhibit exceedingly large negative values of γ , contributing strong anharmonicity and facilitating the 3ph scattering [14,73].

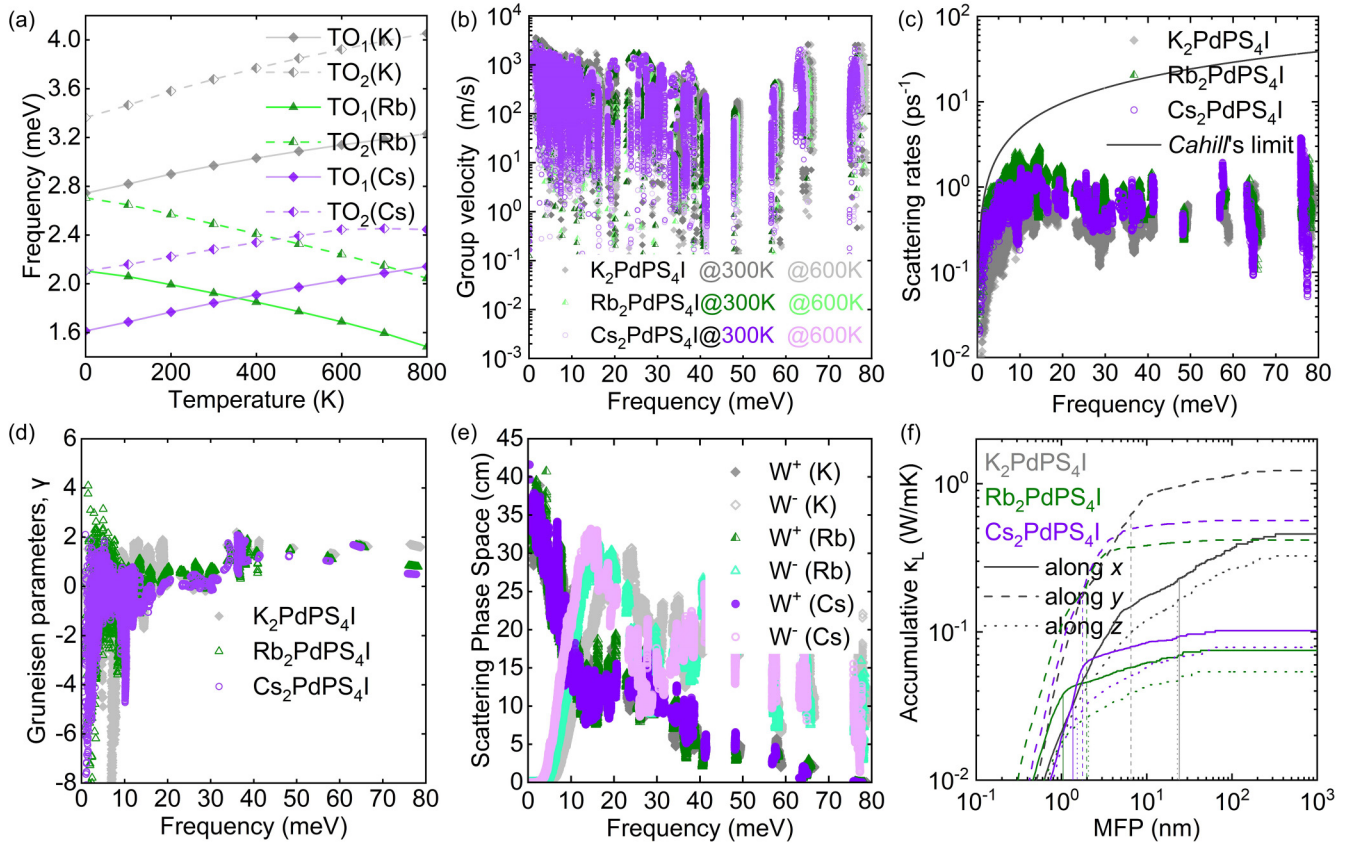


FIG. 4. (a) Phonon frequencies of the lowest TO_1 and TO_2 at Γ in the Brillouin zone as a function of temperature. (b) Comparison of V_{ph} at 300 and 600 K. (c) Scattering rates at 300 K. The black line is the Cahill's limit, assuming the maximum phonon scattering rate of a phonon mode is equal to twice its frequency. (d) γ at 300 K. (e) Calculated energy- and momentum-conserving scattering phase space at 300 K, where the positive and negative upper corner markers represent the combination process and the splitting process of the 3ph scattering, respectively. (f) Cumulative κ_p as a function of MFPs at 300 K. The corresponding perpendicular line represents half of the accumulation process.

As mentioned above, we have performed a visual analysis of the TO_1 modes (see Fig. S6 in the Supplemental Material [65]). The rattlinglike TO_1 modes are correlated with strong anharmonicity and logically hold large atomic displacement parameters. As shown in Fig. S9 in the Supplemental Material [65], the calculated temperature-dependent equivalent isotropic atomic displacement parameters [$U(eq)$] which reflect the magnitude of the atomic displacements, illustrate considerable amplitudes of A and I atoms. These results are well consistent with the weak ionic chemical bonding nature of A and I atoms, which contribute mainly to the strong anharmonicity. Such large $U(eq)$ also illustrate the rattling-like vibrations of the A and I atoms [50]. Heating from 100 to 800 K, the $U(eq)$ of all the atoms increases monotonically, and the increases of I (A) in K_2PdPS_4I , Rb_2PdPS_4I , and Cs_2PdPS_4I are about 0.06 (0.06), 0.09 (0.09), and 0.11 (0.09), respectively. We can see that the $U(eq)$ of A and I in K_2PdPS_4I or Rb_2PdPS_4I are quite similar. Nevertheless, in the Cs-containing system, the displacement parameters of I atoms are larger than those of the Cs atoms. These results indicate that the vibrations of A and I in K_2PdPS_4I and Rb_2PdPS_4I are coordinated, while the vibrations of Cs and I in Cs_2PdPS_4I are relatively isolated. The A and I atoms vibrating synchronously can be regarded as a rigid rattling unit. It is

similar to the Cu dimers rattling mode in CuP_2 manifested to be very anharmonic [85]. Dimer rattling mode strongly scatters the LA phonons, leads to avoiding crossing phenomena, and dominates the reduced κ_L . The isolation of Cs from I is also consistent with the results of COHP analysis. The broken rigid rattling units of Cs and I provide reduced anharmonicity resulting in impaired scattering rates and elevated κ_p .

Last but not least, Fig. 4(e) shows that the scattering phase spaces of the heavier elements are larger than those of the lighter atoms, particularly in the splitting process ($W^-: \lambda \rightarrow \lambda_1 + \lambda_2$) in which the energy of an incident phonon splits into two phonons. This indicates that the harmonic phonon properties are not contributing to the abnormal phonon transport tendency [81]. The anomalous κ_p tendency for our studied compounds stems from the fact that the antibonding of Cs-I breaks the rattling unit of Cs-I, thus weakening the anharmonicity in the crystal.

To assess the potential to reduce κ_p through nanostructuring, we examine the maximum mean-free path (MFP) cumulative κ_p calculated using SCPH+3ph [see Fig. 4(f)]. It can be observed that the phonons in K_2PdPS_4I have the largest MFP. Phonon quasiparticle picture has given that low κ_p can be captured by nanostructures [86]. Thus, the nanostructuring strategy will work best for K_2PdPS_4I .

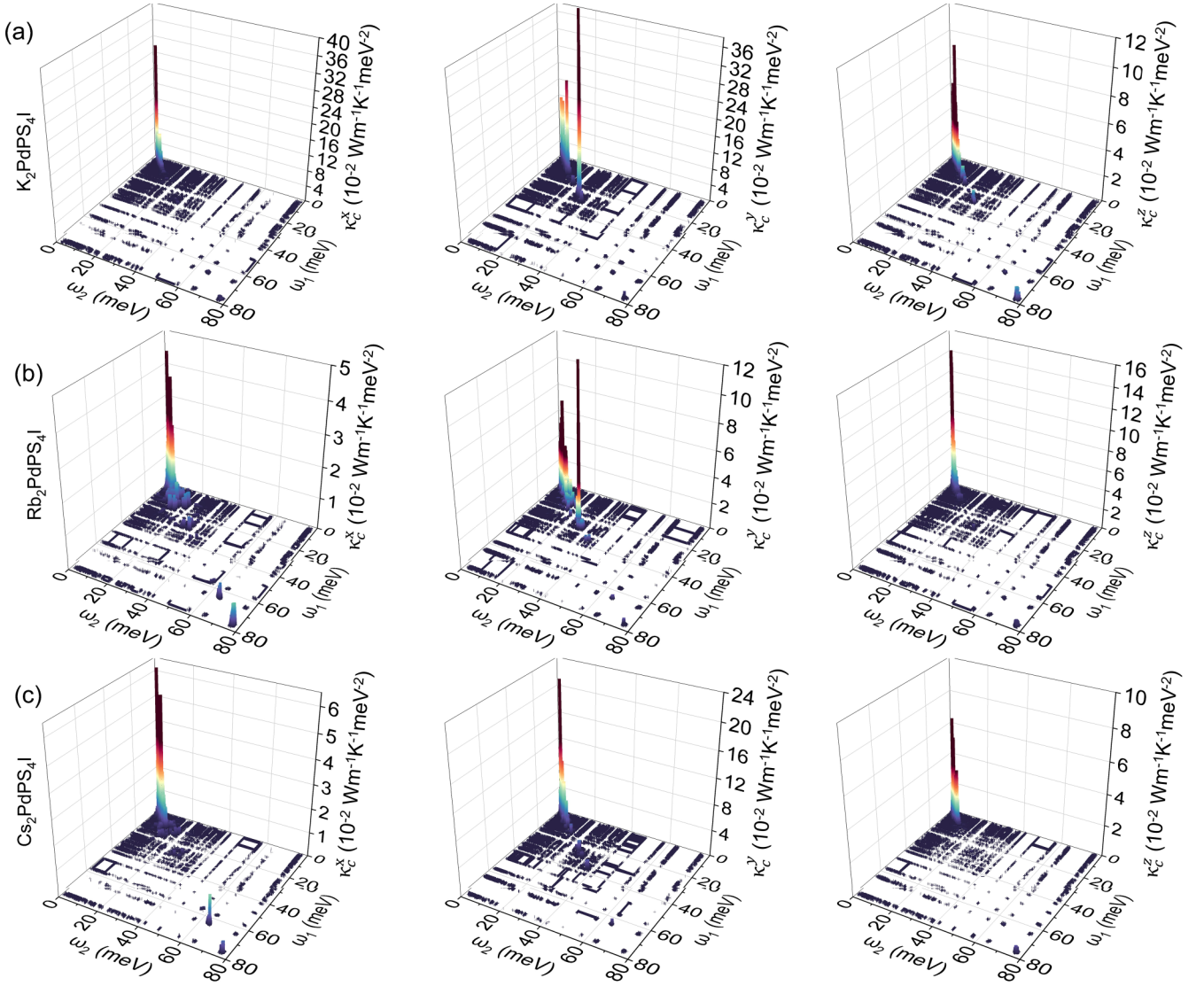


FIG. 5. The mode $\kappa_c(\omega_1, \omega_2)$ of the contribution of the interbranch coherence term is calculated using the frequency of the anharmonic phonon and the eigenvector at 300 K. The points on the diagonal correspond to the quasidegenerate eigenstates ($\omega_1 \approx \omega_2$). These quantities are plotted per cross-sectional area of the Brillouin zone to highlight the phonon frequencies that primarily contribute to the κ_c .

E. Wavelike contributions to κ_L

As mentioned earlier, the invalidity of the particlelike phonon picture (i.e., κ_p) is noted when only the diagonal component of the heat-flux operator is considered [53]. The quasiparticle properties of phonons require a clear dispersion relationship and relatively weak expansion of the phonon states. It is generally understood that the PBTE method is only suitable for systems with high κ_p [87]. For strong anharmonic systems with low κ_L , the strong broadening of the phonon states will generate additional heat transfer channels through the coupling of vibration modes caused by nondiagonal terms in the heat flux operator [53]. In this regard, we consider the OD contribution combined with the renormalized phonon frequency according Eq. (6), to obtain total κ_L [53] as $\kappa_L^{\text{total}} = \kappa_p + \kappa_c$ [88]. The modal κ_c at 300 K is further calculated to show the OD coupling of the vibrational eigenstates. As shown in Fig. 5, the quasidegenerate eigenstates ($\omega_1 \approx \omega_2$) contribute most to κ_c because the smaller the

energy difference between eigenstates, the stronger the wavelike tunneling effect produce [53,87]. The obvious broadening of low-frequency phonons contributes to a non-negligible κ_c in $A_2\text{PdPS}_4\text{I}$.

Due to the similarity of interchain thermal conductivity behavior [Fig. 3(c)], we average the κ_L along the two directions perpendicular to the 1D chain as κ_L^{\parallel} . After taking the κ_c into account, the total κ_L is improved (Fig. 6). The strong anharmonicity results in slightly increasing of the phonon broadening upon heating, and the temperature-induced hardening effect reduces the interbranch space [50], giving wavelike phonon transport a positive temperature-dependent behavior, unlike particle phonon transport (Fig. 3). For all three compounds, the dependences of κ_c on temperature are weakly changed. Such a type of weak temperature-induced dependences have also been found in $\alpha\text{-CsCu}_5\text{Se}_3$ [89] and TlInTe_2 [88]. Due to the κ_p decreases evidently upon heating, the contribution from the coherent channel becomes more and

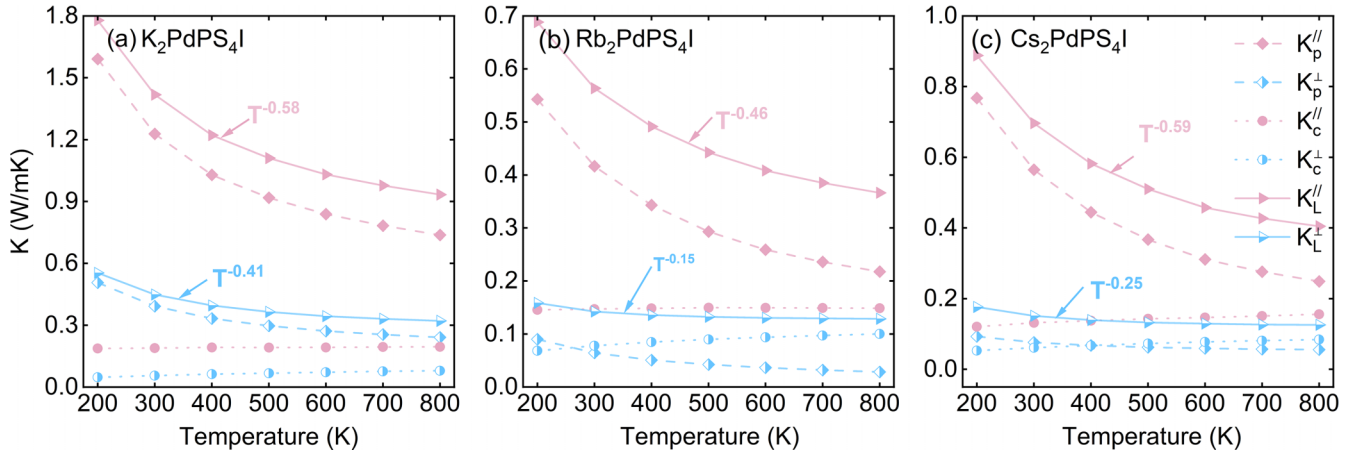


FIG. 6. Calculated κ_L of $A_2\text{PdPS}_4\text{I}$ [$A =$ (a) K, (b) Rb, and (c) Cs] as a function of temperature: particlelike thermal conductivities κ_p , wavelike thermal conductivities κ_c , total κ_L (i.e., $\kappa_L^{\text{total}} = \kappa_p + \kappa_c$) in the direction perpendicular to or parallel to the 1D chains.

more important under high temperatures. To clearly illustrate, we plot the ratios of the contribution of the channels of particle and wavelike transport in Fig. S10 in the Supplemental Material [65]. The results reveal that the coherent scattering cannot be neglected, especially in the direction perpendicular to the 1D chains and for systems of $\text{Rb}_2\text{PdPS}_4\text{I}$ and $\text{Cs}_2\text{PdPS}_4\text{I}$. The interchain κ_c is dominant at high temperature.

F. Electronic structure and electronic transport properties

The exploration of electronic structures is also crucial for understanding low κ_L semiconductors in heat management. The band structures of $A_2\text{PdPS}_4\text{I}$ ($A = \text{K}, \text{Rb}, \text{and Cs}$) calculated with HSE in Fig. 7 exhibit the indirect semiconductor character with band gaps (E_g) of 2.58, 2.63, and 2.68 eV, respectively. Along with increasing the mass of the alkali metal, the E_g increases slightly. The elemental projected band structures and electronic DOS show that the electronic states in the conduction and valence bands are mainly contributed by the S and Pd atoms. The contribution from I atoms is mainly in the range of -2 to -0.5 eV in the valence band.

The replacement alkali metal elements have a weak effect on the band dispersion and their contributions are negligible near the E_F . Therefore, we suggest that the enlarged E_g arises mainly from the expanded lattice volume due to the increased ionic radius. In all three systems, the valence band maximum is rooted at the Γ point. The conduction band maximum is located on the Γ -Y path in both $\text{K}_2\text{PdPS}_4\text{I}$ and $\text{Rb}_2\text{PdPS}_4\text{I}$, while it shifts to the path of U-R for $\text{Cs}_2\text{PdPS}_4\text{I}$.

As indicated in Fig. 8, the bands in the valence band near the E_F show larger dispersion than the bands in the conduction band. The flat conduction bands are indicative of a large effective mass that is not conducive to transport, but they are good for Seebeck coefficients. A theoretical study by Yu *et al.* based on the deformation potential showed the large hole mobility of $241.75 \text{ cm}^2 \text{ s}^{-1} \text{ V}^{-1}$ along y in $\text{K}_2\text{PdS}_4\text{I}$ [36]. Here, we further explore the application of the objects as thermoelectrics. In Fig. S11 in the Supplemental Material [65], we present the room temperature electronic transport properties as functions of the carrier concentrations (σ) in the range of $10^{19} \sim 10^{21} \text{ cm}^{-3}$. The electronic thermal conductivity (κ_e) increases with increasing doping concentration

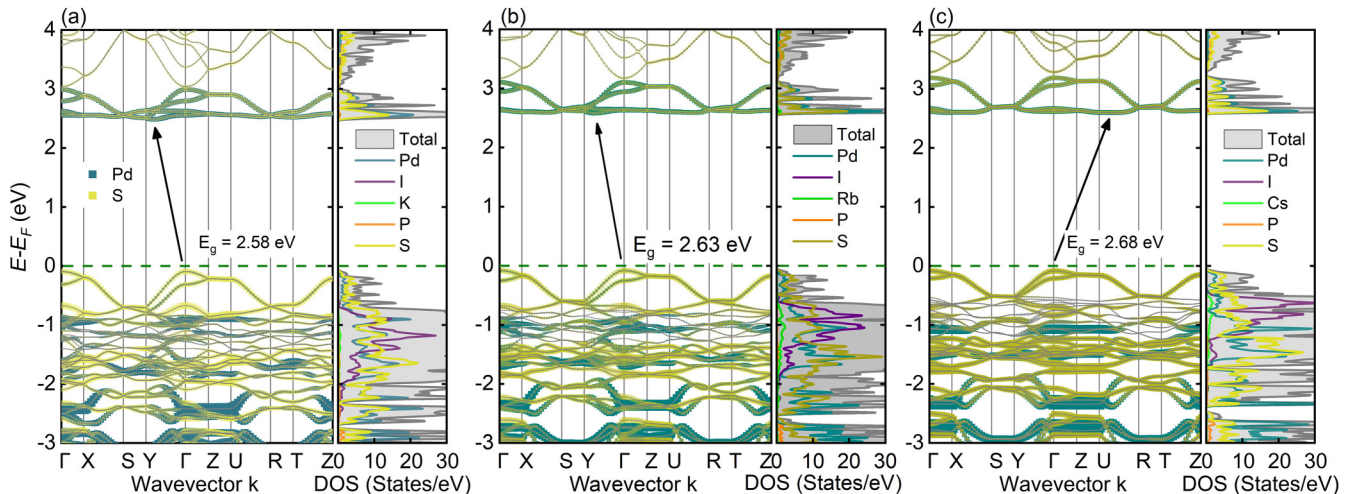


FIG. 7. Electronic structures (projected bands and DOS) of $A_2\text{PdPS}_4\text{I}$ for $A =$ (a) K, (b) Rb, and (c) Cs. The E_F is set to 0 eV.

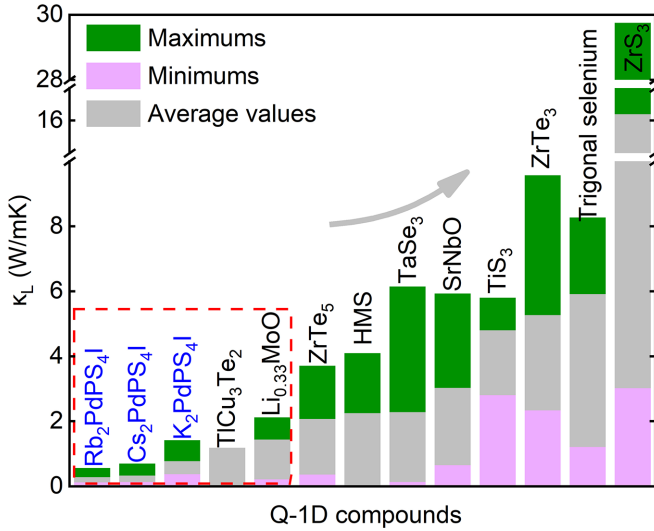


FIG. 8. Extreme and average anisotropic κ_L of Q-1D compound at 300 K, including TICu_3Te_2 [27], $\text{Li}_{0.33}\text{MoO}$ [91], ZrTe_5 [92], HMS [55], TaSe_3 [93], SrNbO [94], TiS_3 [95], ZrTe_3 [93], trigonal selenium [96], and ZrS_3 [97]. The bars are sorted according to average κ_L . The results from this study are marked by the blue font, and the materials containing isolated atoms in the interchain space are framed by the red dotted boxes.

(n) and the majority of contributions are from the y direction (along the covalent 1D chain). Larger Seebeck coefficients are obtained for the n -type doping. The amplitudes of σ in different directions for p -type doping are larger in an order of magnitude than their counterpart for n -type at all doping levels. However, due to opposite changing trends of σ and Seebeck's coefficient (S) with increasing doping concentration, the ideal σ and S are always not obtainable, resulting in a low power factor. Although the thermal conductivities, including both κ_L and κ_e , are larger along the covalent 1D chain lattice, the ZT values are still larger in the y direction than those in the other two directions, due to the better electrical transport properties along the covalent 1D chain compared to the interchain direction (see Fig. S12 in the Supplemental Material [65]). For n -type doping, the maximum ZT value favors room temperature (300 K), with the maximum value (0.20) available in $\text{Cs}_2\text{PdPS}_4\text{I}$. For p -type doping, the maximum ZT value (~ 0.13) is attainable in $\text{K}_2\text{PdPS}_4\text{I}$ at 500 K.

IV. DISCUSSIONS

Utilizing dimensionality reduction and constrained phonon transport, many high-performance bulk thermoelectric materials have been exploited [90]. Compared to layered materials, Q-1D materials with lower dimensions and more confined phonon transport are ideal platforms for slashing the κ_L [17]. Nevertheless, experimental and theoretical studies related to the low κ_L of Q-1D systems are rare. For a broader view, we place our results in the limited context of other Q-1D compounds in Fig. 8, including TICu_3Te_2 [27], $\text{Li}_{0.33}\text{MoO}$ [91], ZrTe_5 [92], higher manganese silicides (HMS) [55], TaSe_3 [93], SrNbO [94], TiS_3 [95], ZrTe_3 [93], trigonal selenium [96], and ZrS_3 [97]. Benefiting from the Q-1D characteristic

structure, the listed compounds all exhibit a high degree of anisotropy, and most of them have ultralow κ_L (< 2.0 W/mK) in a certain direction. What is interesting is that the compounds of our present studied $\text{A}_2\text{PdPS}_4\text{I}$ as well as TICu_3Te_2 [27] and $\text{Li}_{0.33}\text{MoO}$ [91] exhibit a common feature: the presence of interchain isolated atoms (A/I , TI , and Li) in their crystal structures. Based upon our present results and the theoretical background of heat transport [50,53,98–100], several common features for the Q-1D compounds can be obtained: (i) The Q-1D crystal structure dominates the high anisotropy of the κ_L ; (ii) bonding heterogeneity of Q-1D give rise to partially localized low-frequency phonon modes, resulting in low V_{ph} and anharmonicity; (ii) the rattlinglike vibrations of interchain isolated atoms lead to avoid crossing phenomena and provide an optical-acoustic scattering channel, further resulting in the reduction of κ_p ; (iii) the coherent coupling between quasidegenerate phonon eigenstates of the interchain isolated atoms in the low-frequency region make considerable contribution to the wavelike phonon transport and weakly temperature dependency of κ_L .

Other than the merit of using thermoelectric materials, the features of low κ_L and large band gap are basic performance requirements for thermal barrier materials. All our studied palladium thiophosphate $\text{A}_2\text{PdPS}_4\text{I}$ satisfy these conditions. Thus, they may be used as thermal barrier materials. In addition, it is also essential to extend the service life upon damage resistance in real applications, to meet the challenges of harsh environments on the overall mechanical and thermal properties. In particular, to evaluate the damage tolerance, a quasiductility feature, as measured by the Pugh ratio, is required. The Pugh ratio is defined as the ratio of the shear modulus to the bulk modulus G/B and is generally used to predict the quasiductility of materials. When G/B is below the boundary value of 0.571, the material tends to have good inherent quasiductility [101]. In other words, the Pugh's ratio (B/G) should be greater than 1.75, indicating the flexibility of the material. This condition is perfectly satisfied for all our studied three compounds (see Table SI in the Supplemental Material [65]).

V. CONCLUSIONS

In summary, our comprehensive analysis demonstrates that three Q-1D bulk $\text{A}_2\text{PdPS}_4\text{I}$ crystals exhibit strong anharmonicity and ultralow κ_L using first-principles calculations. The temperature-induced frequency shift of phonons has been analyzed by the SCPH method which considers the renormalization of the anharmonic phonons induced by the quartic anharmonicity. Due to the special 1D chains of the crystals, evident anisotropic κ_L is revealed. The low κ_p is mainly originated from the strong anharmonicity of the loose bonding and the rattlinglike vibrations of the A and I atoms, which leads to the strong acoustic-optical phonon scattering, and low-lying and flat optical phonon bands. Besides, the variation in atomic mass of the isoelectronic and isostructural compounds typically results in a uniform change in κ_p . Nonetheless, an anomaly emerges: the $\text{Rb}_2\text{PdPS}_4\text{I}$ with middle mass exhibits the lowest κ_p . From $\text{Rb}_2\text{PdPS}_4\text{I}$ to $\text{Cs}_2\text{PdPS}_4\text{I}$, the unexpected increase of κ_p is observed. In $\text{Rb}_2\text{PdPS}_4\text{I}$, the low-lying rattling phonons from the coordinated vibrations of the A - I units

yield a larger negative value of γ , which can strengthen the phonon anharmonicity, elevate the phonon scattering rates, and consequently diminish the κ_p . For $\text{Cs}_2\text{PdPS}_4\text{I}$, the coordinated vibrations of A and I are broken by the antibonding states and the anharmonicity is debilitated. Furthermore, the shortcomings of the particlelike phonons are compensated by considering the wavelike phonons in calculating the phonon transport. Increasing temperature, strong phonon broadening leads to strong coupling among the coherent phonon eigenstates, resulting in a transition of dominant thermal transport from particlelike wave packet propagation to wavelike tunneling, especially for the directions perpendicular to the 1D chain, thus, well explain the anomalous temperature dependence of the κ_L . Our study reveals the low κ_L caused by multiple mechanisms in a class of Q-1D materials and provides microscopic insights into the dynamics. The loose in-

terchain interactions provide a path to achieve Q-1D ultralow κ_L . At the same time, the tunable anharmonicity by the bonding nature in the units of rattlinglike cooperative vibrations provides a new direction to modulate the phonon anharmonicity and glasslike κ_L in thermal functional materials.

ACKNOWLEDGMENTS

The authors gratefully acknowledge financial support from the National Natural Science Foundation of China (Grants No. 12074381, No. U2330104, No. 52072417 and No. 52072417) and Guang-dong Science & Technology Project (2019QN01C113). The calculations were performed at CSNS Scientific Computing Platform of Institute of High Energy Physics of CAS and GBA Sub-center of National HEP Science Data Center.

-
- [1] W. Liu, K. Yin, Q. Zhang, C. Uher, and X. Tang, Eco-friendly high-performance silicide thermoelectric materials, *Natl. Sci. Rev.* **4**, 611 (2017).
- [2] R. Vaßen, M. O. Jarligo, T. Steinke, D. E. Mack, and D. Stöver, Overview on advanced thermal barrier coatings, *Surf. Coat. Technol.* **205**, 938 (2010).
- [3] V. Apostolopoulou-Kalkavoura, P. Munier, and L. Bergström, Thermally insulating nanocellulose-based materials, *Adv. Mater.* **33**, 2001839 (2021).
- [4] M. Beekman, D. T. Morelli, and G. S. Nolas, Better thermoelectrics through glasslike crystals, *Nat. Mater.* **14**, 1182 (2015).
- [5] B. Poudel, Q. Hao, Y. Ma, Y. Lan, A. Minnich, B. Yu, X. Yan, D. Wang, A. Muto, D. Vashaee, X. Chen, J. Liu, M. S. Dresselhaus, G. Chen, and Z. Ren, High-thermoelectric performance of nanostructured bismuth antimony telluride bulk alloys, *Science* **320**, 634 (2008).
- [6] G. Tan, L. D. Zhao, and M. G. Kanatzidis, Rationally designing high-performance bulk thermoelectric materials, *Chem. Rev.* **116**, 12123 (2016).
- [7] B. Jiang, Y. Yu, J. Cui, X. Liu, L. Xie, J. Liao, Q. Zhang, Y. Huang, S. Ning, B. Jia, B. Zhu, S. Bai, L. Chen, S. J. Pennycook, and J. He, High-entropy-stabilized chalcogenides with high thermoelectric performance, *Science* **371**, 830 (2021).
- [8] S. Lee, K. Esfarjani, T. Luo, J. Zhou, Z. Tian, and G. Chen, Resonant bonding leads to low lattice thermal conductivity, *Nat. Commun.* **5**, 3525 (2014).
- [9] O. Delaire, J. Ma, K. Marty, A. F. May, M. A. McGuire, M. H. Du, D. J. Singh, A. Podlesnyak, G. Ehlers, M. D. Lumsden, and B. C. Sales, Giant anharmonic phonon scattering in PbTe , *Nat. Mater.* **10**, 614 (2011).
- [10] C. W. Li, J. Hong, A. F. May, D. Bansal, S. Chi, T. Hong, G. Ehlers, and O. Delaire, Orbitally driven giant phonon anharmonicity in SnSe , *Nat. Phys.* **11**, 1063 (2015).
- [11] S. Mukhopadhyay, D. Bansal, O. Delaire, D. Perrodin, E. Bourret-Courchesne, D. J. Singh, and L. Lindsay, The curious case of cuprous chloride: Giant thermal resistance and anharmonic quasiparticle spectra driven by dispersion nesting, *Phys. Rev. B* **96**, 100301(R) (2017).
- [12] Y.-K. Jung, I. T. Han, Y. C. Kim, and A. Walsh, Prediction of high thermoelectric performance in the low-dimensional metal halide $\text{Cs}_3\text{Cu}_2\text{I}_5$, *Npj Comput. Mater.* **7**, 51 (2021).
- [13] N. T. Hung and R. Saito, The origin of quantum effects in low-dimensional thermoelectric materials, *Adv. Quantum Technol.* **4**, 2000115 (2020).
- [14] B. Wei, Q. Sun, C. Li, and J. Hong, Phonon anharmonicity: A pertinent review of recent progress and perspective, *Sci. China Phys., Mech. Astron.* **64**, 117001 (2021).
- [15] J. Li, W. Hu, and J. Yang, High-Throughput screening of rattling-induced ultralow lattice thermal conductivity in semiconductors, *J. Am. Chem. Soc.* **144**, 4448 (2022).
- [16] M. Christensen, A. B. Abrahamsen, N. B. Christensen, F. Juranyi, N. H. Andersen, K. Lefmann, J. Andreasson, C. R. Bahl, and B. B. Iversen, Avoided crossing of rattler modes in thermoelectric materials, *Nat. Mater.* **7**, 811 (2008).
- [17] X.-L. Shi and Z.-G. Chen, Quasi-one-dimensional bulk thermoelectrics, *Joule* **7**, 1108 (2023).
- [18] C. Wang and Y. Chen, Highly selective phonon diffusive scattering in superionic layered AgCrSe_2 , *npj Comput. Mater.* **6**, 26 (2020).
- [19] M. Samanta, K. Pal, P. Pal, U. V. Waghmare, and K. Biswas, Localized vibrations of bi bilayer leading to ultralow lattice thermal conductivity and high thermoelectric performance in weak topological insulator n-type BiSe , *J. Am. Chem. Soc.* **140**, 5866 (2018).
- [20] Y. Wu, W. Li, A. Faghaninia, Z. Chen, J. Li, X. Zhang, B. Gao, S. Lin, B. Zhou, A. Jain, and Y. Pei, Promising thermoelectric performance in van der Waals layered SnSe_2 , *Mater. Today Phys.* **3**, 127 (2017).
- [21] L.-D. Zhao, G. Tan, S. Hao, J. He, Y. Pei, H. Chi, H. Wang, S. Gong, H. Xu, V. P. Dravid, C. Uher, G. J. Snyder, C. Wolverton, and M. G. Kanatzidis, Ultrahigh power factor and thermoelectric performance in hole-doped single-crystal SnSe , *Science* **351**, 141 (2016).
- [22] Y. Liu, L. D. Zhao, Y. Liu, J. Lan, W. Xu, F. Li, B. P. Zhang, D. Berardan, N. Dragoë, Y. H. Lin, C. W. Nan, J. F. Li, and H. Zhu, Remarkable enhancement in thermoelectric performance of BiCu_2SeO by Cu deficiencies, *J. Am. Chem. Soc.* **133**, 20112 (2011).

- [23] C. Chang, M. Wu, D. He, Y. Pei, C.-F. Wu, X. Wu, H. Yu, F. Zhu, K. Wang, Y. Chen, L. Huang, J.-F. Li, J. He, and L.-D. Zhao, 3D charge and 2D phonon transports leading to high out-of-plane ZT in n-type SnSe crystals, *Science* **360**, 778 (2018).
- [24] Y.-L. Pei, J. He, J.-F. Li, F. Li, Q. Liu, W. Pan, C. Barreateau, D. Berardan, N. Dragoe, and L.-D. Zhao, High thermoelectric performance of oxyselenides: Intrinsically low thermal conductivity of Ca-doped BiCuSeO, *NPG Asia Mater.* **5**, e47 (2013).
- [25] M. Samanta, T. Ghosh, S. Chandra, and K. Biswas, Layered materials with 2D connectivity for thermoelectric energy conversion, *J. Mater. Chem. A* **8**, 12226 (2020).
- [26] Z. Li, C. Xiao, and Y. Xie, Layered thermoelectric materials: Structure, bonding, and performance mechanisms, *Appl. Phys. Rev.* **9**, 011303 (2022).
- [27] Q. Dong, J. Xiang, Z. Wang, Y. Li, R. Lu, T. Zhang, N. Chen, Y. Huang, Y. Wang, W. Zhu, G. Li, H. Zhao, X. Zheng, S. Zhang, Z. Ren, J. Yang, G. Chen, and P. Sun, A quasi-one-dimensional bulk thermoelectrics with high performance near room temperature, *Sci. Bull. (Beijing)* **68**, 920 (2023).
- [28] D. Yang, W. Yao, Y. Yan, W. Qiu, L. Guo, X. Lu, C. Uher, X. Han, G. Wang, T. Yang, and X. Zhou, Intrinsically low thermal conductivity from a quasi-one-dimensional crystal structure and enhanced electrical conductivity network via Pb doping in SbCrSe₃, *NPG Asia Mater.* **9**, e387 (2017).
- [29] T. Inohara, Y. Okamoto, Y. Yamakawa, A. Yamakage, and K. Takenaka, Large thermoelectric power factor at low temperatures in one-dimensional telluride Ta₄SiTe₄, *Appl. Phys. Lett.* **110**, 183901 (2017).
- [30] K. Kuga, M. Matsunami, S. Singh, S. Nakatsuji, and T. Takeuchi, Simultaneous enhancements of thermopower and electrical conductivity in quasi-one-dimensional α -YbAlB₄ single crystal, *Appl. Phys. Lett.* **119**, 223905 (2021).
- [31] Q.-X. Dong, Y.-F. Huang, L.-B. Zhang, J.-L. Bai, J.-W. Cheng, Q.-Y. Liu, P.-Y. Liu, C.-D. Li, J.-S. Xiang, J.-F. Wang, B.-B. Ruan, Z.-A. Ren, P.-J. Sun, and G.-F. Chen, Enhanced longitudinal and transverse thermopowers at low temperature in quasi-one-dimensional antiferromagnet KMn₆Bi₅, *Appl. Phys. Lett.* **122**, 094104 (2023).
- [32] W. Yoon and H. Yun, Synthesis and structure of a new pentanary one-dimensional palladium thiophosphate, K₂PdPS₄I, *Bull. Korean Chem. Soc.* **42**, 398 (2020).
- [33] F. Xiao, W. Lei, W. Wang, L. Xu, S. Zhang, and X. Ming, Pentagonal two-dimensional noble-metal dichalcogenide PdSSe for photocatalytic water splitting with pronounced optical absorption and ultrahigh anisotropic carrier mobility, *J. Mater. Chem. C* **9**, 7753 (2021).
- [34] F. Xiao, W. Lei, W. Wang, C. Autieri, X. Zheng, X. Ming, and J. Luo, Pressure-induced structural transition, metallization, and topological superconductivity in PdSSe, *Phys. Rev. B* **105**, 115110 (2022).
- [35] F. Xiao, W. Lei, W. Wang, Y. Ma, X. Gong, and X. Ming, Layer-dependent electronic structures and optical properties of two-dimensional PdSSe, *Phys. Chem. Chem. Phys.* **25**, 11827 (2023).
- [36] R. Yu, Q. Ruan, F. Xiao, and X. Ming, First-principles study on the optoelectronic properties of the quasi-one-dimensional flexible semiconductor K₂PdPS₄I, *Results Phys.* **47**, 106396 (2023).
- [37] N. Ma, F. Jia, L. Xiong, L. Chen, Y.-Y. Li, and L.-M. Wu, CsCu₅S₃: Promising thermoelectric material with enhanced phase transition temperature, *Inorg. Chem.* **58**, 1371 (2019).
- [38] N. Ma, Y.-Y. Li, L. Chen, and L.-M. Wu, α -CsCu₅Se₃: Discovery of a low-cost bulk selenide with high thermoelectric performance, *J. Am. Chem. Soc.* **142**, 5293 (2020).
- [39] H. Lin, G. Tan, J.-N. Shen, S. Hao, L.-M. Wu, N. Calta, C. Malliakas, S. Wang, C. Uher, C. Wolverton, and M. G. Kanatzidis, Concerted rattling in CsAg₅Te₃ leading to ultralow thermal conductivity and high thermoelectric performance, *Angew. Chem. Int. Ed.* **55**, 11431 (2016).
- [40] P. E. Blochl, Projector augmented-wave method, *Phys. Rev. B* **50**, 17953 (1994).
- [41] G. Kresse and J. Furthmüller, Efficient iterative schemes for *ab initio* total-energy calculations using a plane-wave basis set, *Phys. Rev. B* **54**, 11169 (1996).
- [42] G. Kresse and J. Furthmüller, Efficiency of *ab initio* total energy calculations for metals and semiconductors using a plane-wave basis set, *Comput. Mater. Sci* **6**, 15 (1996).
- [43] G. Kresse and J. Hafner, *Ab initio* molecular-dynamics simulation of the liquid-metal-amorphous-semiconductor transition in germanium, *Phys. Rev. B* **49**, 14251 (1994).
- [44] B. Hammer, L. B. Hansen, and J. K. Nørskov, Improved adsorption energetics within density-functional theory using revised Perdew-Burke-Ernzerhof functionals, *Phys. Rev. B* **59**, 7413 (1999).
- [45] J. P. Perdew, K. Burke, and M. Ernzerhof, Generalized gradient approximation made simple, *Phys. Rev. Lett.* **77**, 3865 (1996).
- [46] S. Grimme, J. Antony, S. Ehrlich, and H. Krieg, A consistent and accurate *ab initio* parametrization of density functional dispersion correction (DFT-D) for the 94 elements H-Pu, *J. Chem. Phys.* **132**, 154104 (2010).
- [47] F. Zhou, W. Nielson, Y. Xia, and V. Ozoliņš, Lattice anharmonicity and thermal conductivity from compressive sensing of first-principles calculations, *Phys. Rev. Lett.* **113**, 185501 (2014).
- [48] T. Tadano, Y. Gohda, and S. Tsuneyuki, Anharmonic force constants extracted from first-principles molecular dynamics: Applications to heat transfer simulations, *J. Phys.: Condens. Matter* **26**, 225402 (2014).
- [49] T. Tadano and S. Tsuneyuki, Self-consistent phonon calculations of lattice dynamical properties in cubic SrTiO₃ with first-principles anharmonic force constants, *Phys. Rev. B* **92**, 054301 (2015).
- [50] Q.-Y. Xie, P.-F. Liu, J.-J. Ma, L.-M. Wu, K.-W. Zhang, and B.-T. Wang, Microscopic mechanisms of glasslike lattice thermal conductivity in tetragonal α -CsCu₅Se₃, *Phys. Rev. B* **108**, 014302 (2023).
- [51] Q. Li, Y. Cheng, D. Zhao, Y. Huang, X. Wan, and J. Zhou, Intrinsically low lattice thermal conductivity in layered Mn₃Si₂Te₆, *New J. Phys.* **25**, 103020 (2023).
- [52] T. Tadano and S. Tsuneyuki, Quartic anharmonicity of rattlers and its effect on lattice thermal conductivity of clathrates from first principles, *Phys. Rev. Lett.* **120**, 105901 (2018).
- [53] M. Simoncelli, N. Marzari, and F. Mauri, Unified theory of thermal transport in crystals and glasses, *Nat. Phys.* **15**, 809 (2019).
- [54] X. Li, P. F. Liu, E. Zhao, Z. Zhang, T. Guidi, M. D. Le, M. Avdeev, K. Ikeda, T. Otomo, M. Kofu, K. Nakajima, J. Chen,

- L. He, Y. Ren, X. L. Wang, B. T. Wang, Z. Ren, H. Zhao, and F. Wang, Ultralow thermal conductivity from transverse acoustic phonon suppression in distorted crystalline alpha-MgAgSb, *Nat. Commun.* **11**, 942 (2020).
- [55] X. Chen, A. Weathers, J. Carrete, S. Mukhopadhyay, O. Delaire, D. A. Stewart, N. Mingo, S. N. Girard, J. Ma, D. L. Abernathy, J. Yan, R. Sheshka, D. P. Sellan, F. Meng, S. Jin, J. Zhou, and L. Shi, Twisting phonons in complex crystals with quasi-one-dimensional substructures, *Nat. Commun.* **6**, 6723 (2015).
- [56] P. F. Lory, S. Pailhes, V. M. Giordano, H. Euchner, H. D. Nguyen, R. Ramlau, H. Borrmann, M. Schmidt, M. Baitinger, M. Ikeda, P. Tomes, M. Mihalkovic, C. Allio, M. R. Johnson, H. Schober, Y. Sidis, F. Bourdarot, L. P. Regnault, J. Ollivier, S. Paschen, Y. Grin, and M. de Boissieu, Direct measurement of individual phonon lifetimes in the clathrate compound $\text{Ba}_{7.81}\text{Ge}_{40.67}\text{Au}_{5.33}$, *Nat. Commun.* **8**, 491 (2017).
- [57] S. Mukhopadhyay, D. S. Parker, B. C. Sales, A. A. Puretzy, M. A. McGuire, and L. Lindsay, Two-channel model for ultralow thermal conductivity of crystalline Tl_3VSe_4 , *Science* **360**, 1455 (2018).
- [58] Y. Le Page and P. Saxe, Symmetry-general least-squares extraction of elastic data for strained materials from ab initio calculations of stress, *Phys. Rev. B* **65**, 104104 (2002).
- [59] A. M. Ganose, J. Park, A. Faghaninia, R. Woods-Robinson, K. A. Persson, and A. Jain, Efficient calculation of carrier scattering rates from first principles, *Nat. Commun.* **12**, 2222 (2021).
- [60] M. Born, Zur Quantenmechanik der Stoßvorgänge, *Z. Phys.* **37**, 863 (1926).
- [61] H. Fröhlich, Electrons in lattice fields, *Adv. Phys.* **3**, 325 (1954).
- [62] X. Wu, D. Vanderbilt, and D. R. Hamann, Systematic treatment of displacements, strains, and electric fields in density-functional perturbation theory, *Phys. Rev. B* **72**, 035105 (2005).
- [63] L. Schimka, R. Gaudoin, J. Klimeš, M. Marsman, and G. Kresse, Lattice constants and cohesive energies of alkali, alkaline-earth, and transition metals: Random phase approximation and density functional theory results, *Phys. Rev. B* **87**, 214102 (2013).
- [64] R. Sahara, T. Shishido, A. Nomura, K. Kudou, S. Okada, V. Kumar, K. Nakajima, and Y. Kawazoe, First-principles study of the structural, electronic, and elastic properties of $\text{RRh}_3\text{B}_x\text{C}_{1-x}$ ($R = \text{Sc}$ and Y), *Phys. Rev. B* **76**, 024105 (2007).
- [65] See Supplemental Material at <http://link.aps.org/supplemental/10.1103/PhysRevB.109.245202> for the energy fluctuations with respect to AIMD steps, elastic modulus, anisotropic mechanical properties, COHP of the nearest-neighbor atomic pairs, the electron local function, avoided crossing modes in the local enlarged phonon spectra, vibration patterns of TO_1 at the Γ point, convergence tests of the calculated κ_p concerning q -point mesh, projections of Grüneisen parameters of the phonon dispersions, temperature-dependent equivalent isotropic displacement parameter, the ratios of κ_c/κ_p , electronic thermal conductivity (κ_e), Seebeck coefficient (S), and electrical conductivity (σ), as a function of carrier concentration, zT for $\text{A}_2\text{PdPS}_4\text{I}$.
- [66] F. Mouhat and F.-X. Coudert, Necessary and sufficient elastic stability conditions in various crystal systems, *Phys. Rev. B* **90**, 224104 (2014).
- [67] A. Das, K. Pal, P. Acharyya, S. Das, K. Maji, and K. Biswas, Strong antibonding I(p)-Cu(d) states lead to intrinsically low thermal conductivity in CuBiI_4 , *J. Am. Chem. Soc.* **145**, 1349 (2023).
- [68] G. N. Greaves, A. L. Greer, R. S. Lakes, and T. Rouxel, Poisson's ratio and modern materials, *Nat. Mater.* **10**, 823 (2011).
- [69] S. F. Pugh, XCII. Relations between the elastic moduli and the plastic properties of polycrystalline pure metals, *London Edinburgh Dublin Philos. Mag. J. Sci.* **45**, 823 (2009).
- [70] C. Ott, F. Reiter, M. Baumgartner, M. Pielmeier, A. Vogel, P. Walke, S. Burger, M. Ehrenreich, G. Kieslich, D. Daisenberger, J. Armstrong, U. K. Thakur, P. Kumar, S. Chen, D. Donadio, L. S. Walter, R. T. Weitz, K. Shankar, and T. Nilges, Flexible and ultrasoft inorganic 1D semiconductor and heterostructure systems based on SnIP , *Adv. Funct. Mater.* **29**, 1900233 (2019).
- [71] J. Zhang, D. He, H. Jiang, X. Xia, Y. Gao, and Z. Huang, Remarkable thermoelectric performance in K_2CdPb crystals with 1D building blocks via structure particularity and bond heterogeneity, *ACS Appl. Energy Mater.* **5**, 5146 (2022).
- [72] D. Sarkar, K. Dolui, V. Taneja, A. Ahad, M. Dutta, S. O. Manjunatha, D. Swain, and K. Biswas, Chemical bonding tuned lattice anharmonicity leads to a high thermoelectric performance in cubic AgSnSbTe_3 , *Angew. Chem. Int. Ed Engl.* **62**, e202308515 (2023).
- [73] C. W. Li, O. Hellman, J. Ma, A. F. May, H. B. Cao, X. Chen, A. D. Christianson, G. Ehlers, D. J. Singh, B. C. Sales, and O. Delaire, Phonon self-energy and origin of anomalous neutron scattering spectra in SnTe and PbTe thermoelectrics, *Phys. Rev. Lett.* **112**, 175501 (2014).
- [74] J. Zheng, D. Shi, S. Liu, Y. Yang, C. Lin, Z. Chang, R. Guo, and B. Huang, Effects of high-order anharmonicity on anomalous lattice dynamics and thermal transport in fully filled skutterudite $\text{YbFe}_4\text{Sb}_{12}$, *Phys. Rev. Mater.* **6**, 093801 (2022).
- [75] T. Yue, P. Sui, Y. Zhao, J. Ni, S. Meng, and Z. Dai, Theoretical prediction of mechanics, transport, and thermoelectric properties of full Heusler compounds Na_2KSb and X_2CsSb ($X = \text{K}, \text{Rb}$), *Phys. Rev. B* **105**, 184304 (2022).
- [76] K. Biswas, J. He, I. D. Blum, C. I. Wu, T. P. Hogan, D. N. Seidman, V. P. Dravid, and M. G. Kanatzidis, High-performance bulk thermoelectrics with all-scale hierarchical architectures, *Nature (London)* **489**, 414 (2012).
- [77] Y. Zhou and L. D. Zhao, Promising thermoelectric bulk materials with 2D structures, *Adv. Mater.* **29**, 1702676 (2017).
- [78] I. T. Witting, T. C. Chasapis, F. Ricci, M. Peters, N. A. Heinz, G. Hautier, and G. J. Snyder, The thermoelectric properties of bismuth telluride, *Adv. Electron. Mater.* **5**, 1800904 (2019).
- [79] R. W. Keyes, High-Temperature thermal conductivity of insulating crystals: Relationship to the melting point, *Phys. Rev.* **115**, 564 (1959).
- [80] R. Peierls, Zur kinetischen theorie der wärmeleitung in kristallen, *Ann. Phys.* **395**, 1055 (1929).
- [81] L. Elalfy, D. Music, and M. Hu, Metavalent bonding induced abnormal phonon transport in diamondlike structures: Beyond conventional theory, *Phys. Rev. B* **103**, 075203 (2021).

- [82] D. G. Cahill, S. K. Watson, and R. O. Pohl, Lower limit to the thermal conductivity of disordered crystals, *Phys. Rev. B* **46**, 6131 (1992).
- [83] J. Callaway, Model for lattice thermal conductivity at low temperatures, *Phys. Rev.* **113**, 1046 (1959).
- [84] M. T. Dove, Z. Wei, A. E. Phillips, D. A. Keen, and K. Refson, Which phonons contribute most to negative thermal expansion in ScF_3 ?, *APL Mater.* **11**, 041130 (2023).
- [85] J. Qi, B. Dong, Z. Zhang, Z. Zhang, Y. Chen, Q. Zhang, S. Danilkin, X. Chen, J. He, L. Fu, X. Jiang, G. Chai, S. Hiroi, K. Ohara, Z. Zhang, W. Ren, T. Yang, J. Zhou, S. Osami, J. He, D. Yu, B. Li, and Z. Zhang, Dimer rattling mode induced low thermal conductivity in an excellent acoustic conductor, *Nat. Commun.* **11**, 5197 (2020).
- [86] T. Yue, Y. Zhao, J. Ni, S. Meng, and Z. Dai, Microscopic mechanism of low lattice thermal conductivity in natural superlattice materials BaXYF ($X = \text{Cu, Ag}$; $Y = \text{Se, Te}$) including fully quartic anharmonicity, *Phys. Rev. B* **107**, 024301 (2023).
- [87] Y. Xia, V. I. Hegde, K. Pal, X. Hua, D. Gaines, S. Patel, J. He, M. Aykol, and C. Wolverton, High-Throughput study of lattice thermal conductivity in binary rocksalt and zinc blende compounds including higher-order anharmonicity, *Phys. Rev. X* **10**, 041029 (2020).
- [88] K. Pal, Y. Xia, and C. Wolverton, Microscopic mechanism of unusual lattice thermal transport in TlInTe_2 , *Npj Comput. Mater.* **7**, 5 (2021).
- [89] Q. Y. Xie, J. J. Ma, Q. Y. Liu, P. F. Liu, P. Zhang, K. W. Zhang, and B. T. Wang, Low thermal conductivity and high performance anisotropic thermoelectric properties of $X\text{Se}$ ($X = \text{Cu, Ag, Au}$) monolayers, *Phys. Chem. Chem. Phys.* **24**, 7303 (2022).
- [90] X.-L. Shi, J. Zou, and Z.-G. Chen, Advanced thermoelectric design: From materials and structures to devices, *Chem. Rev.* **120**, 7399 (2020).
- [91] S. Moshfeghyeganeh, A. N. Cote, J. J. Neumeier, and J. L. Cohn, Anisotropic transport in the quasi-one-dimensional semiconductor $\text{Li}_{0.33}\text{MoO}_3$, *J. Appl. Phys.* **119**, 095105 (2016).
- [92] J. Zhu, T. Feng, S. Mills, P. Wang, X. Wu, L. Zhang, S. T. Pantelides, X. Du, and X. Wang, Record-Low and anisotropic thermal conductivity of a quasi-one-dimensional bulk ZrTe_5 single crystal, *ACS Appl. Mater. Interfaces* **10**, 40740 (2018).
- [93] T. Debnath, B. Debnath, and R. K. Lake, Thermal conductivity of the quasi-one-dimensional materials TaSe_3 and ZrTe_3 , *Phys. Rev. Mater.* **5**, 034010 (2021).
- [94] W. Kobayashi, Y. Hayashi, M. Matsushita, Y. Yamamoto, I. Terasaki, A. Nakao, H. Nakao, Y. Murakami, Y. Moritomo, H. Yamauchi, and M. Karppinen, Anisotropic thermoelectric properties associated with dimensional crossover in quasi-one-dimensional $\text{SrNbO}_{3.4+d}$ ($d \sim 0.03$), *Phys. Rev. B* **84**, 085118 (2011).
- [95] H. Liu, X. Yu, K. Wu, Y. Gao, S. Tongay, A. Javey, L. Chen, J. Hong, and J. Wu, Extreme in-plane thermal conductivity anisotropy in titanium trisulfide caused by heat-carrying optical phonons, *Nano Lett.* **20**, 5221 (2020).
- [96] H. Peng, D. Hou, and G. Chen, Quasi-one-dimensional thermal transport in trigonal selenium crystal, *J. Phys.: Condens. Matter* **33**, 455402 (2021).
- [97] C. Wang, C. Zheng, and G. Gao, Bulk and monolayer ZrS_3 as promising anisotropic thermoelectric materials: A comparative study, *J. Phys. Chem. C* **124**, 6536 (2020).
- [98] Z. Tong, Y. Zhang, A. Pecchia, C. Yam, L. Zhou, T. Dumitrica, and T. Frauenheim, Predicting the lattice thermal conductivity in nitride perovskite LaWN_3 from *ab initio* lattice dynamics, *Adv Sci (Weinh)* **10**, e2205934 (2023).
- [99] Z. Tong, A. Pecchia, C. Yam, T. Dumitrica, and T. Frauenheim, Glasslike transport dominates ultralow lattice thermal conductivity in modular crystalline $\text{Bi}_4\text{O}_4\text{SeCl}_2$, *Nano Lett.* **23**, 9468 (2023).
- [100] T. Yue, Y. Zhao, J. Ni, S. Meng, and Z. Dai, Strong quartic anharmonicity, ultralow thermal conductivity, high band degeneracy and good thermoelectric performance in Na_2TlSb , *Npj Comput. Mater.* **9**, 17 (2023).
- [101] Y. Liu, V. R. Cooper, B. Wang, H. Xiang, Q. Li, Y. Gao, J. Yang, Y. Zhou, and B. Liu, Discovery of ABO_3 perovskites as thermal barrier coatings through high-throughput first principles calculations, *Mater. Res. Lett.* **7**, 145 (2019).